(Nearly) Model-independent constraints on the neutral hydrogen fraction in the intergalactic medium at z 5-7 using dark pixel fractions in Ly-α and Ly-β forests

Jin, X.; Yang, J.; Fan, X.; Wang, F.; Bañados, E.; Bian, F.; ... ; Walter, F.

(Nearly) Model-independent Constraints on the Neutral Hydrogen Fraction in the Intergalactic Medium at $z \sim 5$–7 Using Dark Pixel Fractions in Lyα and Lyβ Forests

Xiangyu Jin[1] , Jinyi Yang[1,10] , Xiaohui Fan[1] , Feige Wang[1,11] , Eduardo Bañados[2] , Fuyan Bian[3] ,
Frederick B. Davies[2] , Anna-Christina Eilers[4,11] , Emanuele Paolo Farina[5] , Joseph F. Hennawi[6,7] , Fabio Pacucci[8,9] ,
Bram Venemans[7] , and Fabian Walter[2]

[1] Steward Observatory, University of Arizona, 933 N. Cherry Avenue, Tucson, AZ 85719, USA
[2] Max Planck Institut für Astronomie, Königstuhl 17, D-69117 Heidelberg, Germany
[3] European Southern Observatory, Alonso de Córdova 3107, Casilla 19001, Vitacura, Santiago 19, Chile
[4] MIT Kavli Institute for Astrophysics and Space Research, 77 Massachusetts Avenue, Cambridge, MA 02139, USA
[5] Gemini Observatory, NSF's NOIRLab, 670 N A'ohoku Place, Hilo, HI 96720, USA
[6] Department of Physics, Broida Hall, University of California, Santa Barbara, CA 93106-9530, USA
[7] Leiden Observatory, Leiden University, P.O. Box 9513, NL-2300 RA Leiden, The Netherlands
[8] Center for Astrophysics | Harvard & Smithsonian, Cambridge, MA 02138, USA
[9] Black Hole Initiative, Harvard University, Cambridge, MA 02138, USA

Abstract

Cosmic reionization was the last major phase transition of hydrogen from neutral to highly ionized in the intergalactic medium (IGM). Current observations show that the IGM is significantly neutral at $z > 7$ and largely ionized by $z \sim 5.5$. However, most methods to measure the IGM neutral fraction are highly model dependent and are limited to when the volume-averaged neutral fraction of the IGM is either relatively low ($\overline{x}_{\mathrm{H\,I}} \lesssim 10^{-3}$) or close to unity ($\overline{x}_{\mathrm{H\,I}} \sim 1$). In particular, the neutral fraction evolution of the IGM at the critical redshift range of $z = 6$–7 is poorly constrained. We present new constraints on $\overline{x}_{\mathrm{H\,I}}$ at $z \sim 5.1$–6.8 by analyzing deep optical spectra of 53 quasars at $5.73 < z < 7.09$. We derive model-independent upper limits on the neutral hydrogen fraction based on the fraction of "dark" pixels identified in the Lyα and Lyβ forests, without any assumptions on the IGM model or the intrinsic shape of the quasar continuum. They are the first model-independent constraints on the IGM neutral hydrogen fraction at $z \sim 6.2$–6.8 using quasar absorption measurements. Our results give upper limits of $\overline{x}_{\mathrm{H\,I}}(z = 6.3) < 0.79 \pm 0.04$ (1σ), $\overline{x}_{\mathrm{H\,I}}(z = 6.5) < 0.87 \pm 0.03$ (1σ), and $\overline{x}_{\mathrm{H\,I}}(z = 6.7) < 0.94^{+0.06}_{-0.09}$ (1σ). The dark pixel fractions at $z > 6.1$ are consistent with the redshift evolution of the neutral fraction of the IGM derived from Planck 2018.

Unified Astronomy Thesaurus concepts: Reionization (1383); Intergalactic medium (813); Cosmology (343)

1. Introduction

Cosmic reionization was the epoch that started when UV photons from the first luminous sources ionized neutral hydrogen in the intergalactic medium (IGM) and ended the dark ages. Reionization was the last major phase transition of hydrogen in the IGM, influencing almost every baryon in the universe. Determining when and how the reionization happened can help us to understand early structure formation and the properties of the first luminous sources in the universe. The optical depth measured from the cosmic microwave background provides an integrated constraint on reionization, and the Planck 2018 results infer a midpoint redshift of reionization is $z_{\mathrm{re}} = 7.7 \pm 0.8$ (Planck Collaboration et al. 2020). However, the detailed temporal evolution of the IGM neutral fraction, as well as its spatial variation, during the reionization era require other measurements from discrete astrophysical sources.

The redshift evolution of the IGM neutral fraction during the reionization can be constrained by various observations. The Lyα and Lyβ effective optical depth measurements suggest that the IGM is highly ionized (volume-averaged IGM neutral fraction $\overline{x}_{\mathrm{H\,I}} \lesssim 10^{-4}$) at $z \sim 5.5$, while the tail end of reionization likely extends to as low as $z \sim 5.3$ (e.g., Fan et al. 2006; Becker et al. 2015; Bosman et al. 2018, 2021; Eilers et al. 2018, 2019; Yang et al. 2020a). At $z \gtrsim 6$, the emergence of complete Gunn–Peterson troughs in quasar spectra indicates a rapid increase in the neutral fraction of the IGM. At the same time, the quasar Lyα and Lyβ forests become saturated, and their optical depth is no longer sensitive to the ionization state of the IGM. Close to the midpoint of reionization, the Gunn–Peterson optical depth is high enough to have strong off-resonance scattering in the form of IGM damping wings in the quasar proximity zone (Miralda-Escudé 1998). Damping wing measurements indicates the IGM is significantly neutral at $z \sim 7.1$–7.6 ($\overline{x}_{\mathrm{H\,I}} \sim 0.2$–0.7; Greig et al. 2017, 2019, 2022; Bañados et al. 2018; Davies et al. 2018; Wang et al. 2020; Yang et al. 2020b). This leaves a gap in the IGM neutral fraction measurements between $z \sim 6$–7, a critical period in the reionization history when the IGM is likely experiencing the most rapid evolution.

Apart from Lyα effective optical depth and IGM damping wings, high-redshift quasars can provide other constraints on $\overline{x}_{\mathrm{H\,I}}$: (1) The covering fraction of "dark" pixels, present in the Lyα and Lyβ forests, can constrain $\overline{x}_{\mathrm{H\,I}}$ as model-independent upper limits (Mesinger 2010; McGreer et al. 2011, 2015). McGreer et al. (2015) show that $\overline{x}_{\mathrm{H\,I}} < 0.04 + 0.05$ at $z = 5.6$ (1σ), and $\overline{x}_{\mathrm{H\,I}} < 0.06 + 0.05$ at $z = 5.8$ (1σ). (2) The length

---

distribution of long "dark" gaps in Lyα and Lyβ forests can provide model-dependent constraints on $\bar{x}_{\rm H\,I}$ by comparing with predictions from reionization models (Mesinger 2010). Zhu et al. (2021) suggest that the dark gap statistics in Lyα forests favor late reionization models in which reionization ends below $z \sim 6$, and Zhu et al. (2022) constrain $\bar{x}_{\rm H\,I} < 0.05$, 0.17 and 0.29 at $z = 5.55$, 5.75, and 5.95 from the length distribution of dark gaps in Lyα and Lyβ forests. (3) Mean free path of ionizing photons measured from composite quasar spectra can also be used to constrain $\bar{x}_{\rm H\,I}$ by comparing mean free paths with predicted results of reionization models (Worseck et al. 2014; Becker et al. 2021). Mean free paths measured in Becker et al. (2021) favor late reionization models in which $\bar{x}_{\rm H\,I} = 0.2$ at $z = 6$. (4) The size of quasar proximity zones can infer $\bar{x}_{\rm H\,I}$ (e.g., Fan et al. 2006; Carilli et al. 2010; Calverley et al. 2011; Venemans et al. 2015; Eilers et al. 2017) though the results are dependent on quasar lifetimes.

The process of reionization can also be constrained by high-z galaxy observations through various methods: (1) the fraction of Lyα emitters (LAEs) in the broadband selected Lyman break galaxies (e.g., Stark et al. 2010; Pentericci et al. 2011; Schenker et al. 2014); (2) the clustering (angular correlation function) of LAEs (e.g., Sobacchi & Mesinger 2015; Ouchi et al. 2018); (3) the distribution of Lyα equivalent width of LAEs (e.g., Mason et al. 2018, 2019; Hoag et al. 2019; Jung et al. 2020); and (4) the evolution of Lyα luminosity functions (e.g., Konno et al. 2014, 2018; Itoh et al. 2018; Morales et al. 2021).

Almost all the methods of measuring the neutral fraction of the IGM discussed above are model dependent: they rely on a number of assumptions, including models of IGM density distributions, reconstruction of quasar intrinsic spectra, quasar lifetime, or intrinsic evolution of Lyα emission in galaxies. In contrast, the dark pixel method gives the least model-dependent constraints on $\bar{x}_{\rm H\,I}$. This method was first proposed in Mesinger (2010), which uses the covering fraction of dark pixels of ~ 3 Mpc size as simple upper limits on $\bar{x}_{\rm H\,I}$ since both preoverlap and postoverlap neutral patches in the IGM can cause dark pixels. This method thus hardly relies neither on the modeling of the intrinsic emission of the quasar nor on IGM models. The dark pixel method only assumes the size of neutral patches is bigger than 3 Mpc; therefore, it can be used as a nearly model-independent probe of reionization. The drawback is that without assuming a specific IGM density distribution, the dark pixel fraction is strictly an upper limit on the neutral fraction. Using the covering fraction of dark pixels, McGreer et al. (2015) have derived stringent constraints on $\bar{x}_{\rm H\,I}$ at $z < 6$ based a sample of 22 quasars at $5.73 < z < 6.42$.

In this work, we expand these studies by using a much larger sample of 53 quasars and expand the redshift range to $5.73 < z < 7.09$. This allows us to derive new constraints on $\bar{x}_{\rm H\,I}$ at $5.1 < z < 6.8$ by measuring the covering fraction of dark pixels. In particular, it provides reliable upper limits of $\bar{x}_{\rm H\,I}$ at $z > 6.2$ for the first time. This paper is organized as follows: we present the data set used in our analysis in Section 2, the dark pixel method in Section 3, results and discussion in Section 4, and our conclusion in Section 5. Throughout this paper, we adopt a flat ΛCDM cosmology with cosmological parameters $H_0 = 70\ {\rm km\ s}^{-1}\ {\rm Mpc}^{-1}$ and $\Omega_{\rm M} = 0.3$.

2. Data Preparation

The spectra of the 53 quasars used in this work include most of the spectra presented in McGreer et al. (2011, 2015) and in

Yang et al. (2020a). The quasar sample in McGreer et al. (2011, 2015) includes 29 spectra of 22 quasars at $5.73 < z < 6.42$, obtained with Keck II Telescope/Echellette Spectrograph and Imager (ESI), Magellan Baade Telescope/ Magellan Echellette (MagE) Spectrograph, Multi-Mirror Telescope (MMT)/Red Channel Spectrograph, and Very Large Telescope (VLT)/X-Shooter. The quasar sample in Yang et al. (2020a) includes 35 spectra of 32 quasars at $6.31 < z < 7.00$ obtained with VLT/X-Shooter, Keck II/DEep Imaging Multi-Object Spectrograph (DEIMOS), Keck I/Low Resolution Imaging Spectrometer (LRIS), Gemini/Gemini Multi-Object Spectrographs (GMOS), Large Binocular Telescope (LBT)/ Multi-Object Double CCD Spectrographs (MODS), and MMT/BINOSPEC. For the data reduction of these spectra, we refer the reader to McGreer et al. (2011, 2015) and Yang et al. (2020a) for more details. In addition to the spectra in McGreer et al. (2011, 2015) and Yang et al. (2020a), we have also included new VLT/X-Shooter spectra for quasars J0252–0503 ($z = 7.00$) and J2211–6320 ($z = 6.84$) in our study, both taken in 2019, and an archival VLT/X-Shooter spectrum for quasar J1120+0641 at $z = 7.085$ (Mortlock et al. 2011), taken in 2011 (Barnett et al. 2017). For the new VLT/ X-Shooter spectra of J0252–0503 and J2211–6320, we perform the data reduction for bias subtracting, flat-fielding, and flux calibration with PypeIt (Prochaska et al. 2020a, 2020b), following the standard thread.[12] We present these two VLT/X-Shooter spectra in Figure 1.

We summarize the optical spectroscopy of all 53 quasars in Table 1, in descending order of redshift. We show the redshift distribution of all quasars and the redshift range of Lyα and Lyβ forests used in our data pixel fraction analysis in Figure 2.

For objects with multiple spectra, we use the histogram method to stack these spectra to improve the signal-to-noise ratio (S/N): we first set a common wavelength grid, based on the spectrum with the lowest spectral resolution among all the spectra of the same object. Then we use the inverse variance weighting to calculate the flux and the spectral uncertainty of each pixel on the common wavelength grid to obtain a stack spectrum.

For the range of the Lyα forest used in our analysis, we choose the blue cutoff at 1050 Å in the rest frame to exclude the possible emission from O VI λ1033 (Bosman et al. 2021). We choose a red cutoff at 1176 Å in the rest frame to avoid possible contamination from the quasar proximity zone.[13] For the wavelength coverage of the Lyβ forest, we select a blue cutoff at 975 Å in the rest frame to avoid contamination from Lyman γ forests. We also match the red cut of the Lyβ forest to the same absorption redshift as the red cut of the Lyα forest (i.e., $1176\ \mathring{A} \times \lambda_{\rm Ly\beta}/\lambda_{\rm Ly\alpha}$ in the rest frame, where $\lambda_{\rm Ly\alpha} = 1215.7$ Å and $\lambda_{\rm Ly\beta} = 1025.7$ Å are the rest wavelengths of Lyα and Lyβ), resulting in a wavelength range of 975–992.2 Å.

To minimize the contamination of strong sky emission lines (mainly OH emission) in our analysis, we first apply a median filter of 3 pixels to smooth the spectrum and then mask pixels that are above 3σ in both flux density and spectral uncertainty than the smoothed spectrum. We reject pixels with S/N < -5 caused by oversubtraction of sky. Due to the sky O_2 emission (Osterbrock et al. 1996), we also mask the S/N > 2 pixels in the observed range of 8620–8680 Å. This may exclude real

---

[12] https://pypeit.readthedocs.io/en/release/cookbook.html
[13] A rest-frame wavelength of 1176 Å is corresponding to 14.9 proper Mpc from a $z = 5.73$ quasar and to 11.3 proper Mpc from a $z = 7.09$ quasar.
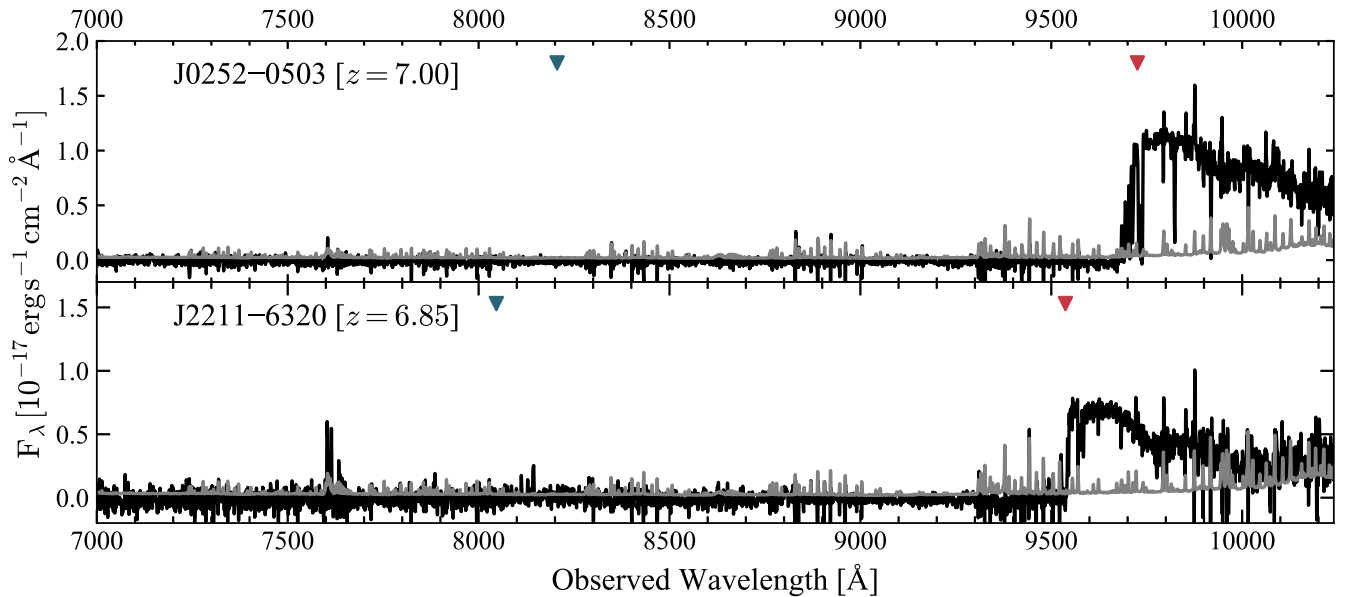
Figure 1. VLT/X-Shooter spectra of J0252–0503 and J2211–6320 in the observed wavelength. The original spectrum is shown by the black line, and spectral uncertainty is in gray. The observed wavelengths of Lyα and Lyβ emission lines are denoted by the red and blue triangles, respectively. Both spectra are smoothed with a median filter of 5 pixels for better visualization.

transmission spikes, but S/N > 2 pixels within this region cannot be identified as transmission spikes precisely based on the current data quality. Eilers et al. (2019) showed that the metal absorption line contribution is negligible at $z \sim 6$, and we thus do not correct them in our analysis.

For some VLT/X-Shooter spectra in our study (especially at the high-redshift end), the sky background level is not precisely subtracted, resulting in a "zero" flux offset in these spectra. This flux floor is removed empirically as follows: After skyline masking, we first investigate the flux distribution of pixels in the Lyα forest. Then we perform 2σ sigma clipping on the pixel flux until convergence of the mean and the median flux is achieved. Figure 3 shows the flux distribution of pixels in the Lyα forest as the black histogram from the J1120+0641 VLT/X-Shooter spectrum. The median flux from the sigma-clipped pixels is denoted by the vertical dashed line, and the 2σ range from the sigma clipping is represented by the gray shaded region. We use the median flux of sigma-clipped pixels to correct the zero flux level for all VLT/X-Shooter spectra of quasars. The average flux correction in transmitted flux is ~0.08%–4%.

3. Methods

To improve the dynamic range of the spectrum, we follow a similar method as the method described in McGreer et al. (2011) to perform spectral binning. The size of each binned pixel is 3.3 Mpc in the comoving distance (i.e., 3.3 cMpc), following McGreer et al. (2011, 2015). To avoid any contamination caused by residual skylines in the spectrum, we first identify the local minima in the 1σ spectral uncertainty in the Lyα and Lyβ forests with argrelextrema in Scipy (Virtanen et al. 2020) and an order of 3, which identifies those local minima that are less than their three neighboring pixels in the spectral uncertainty. We place the 3.3 cMpc pixels centered at those local minima until the interval between any two adjacent pixels is less than 3.3 cMpc. We then use the inverse variance weighting to calculate the flux and the spectral uncertainty of each 3.3 cMpc binned pixel. As an example,

Figure 4 shows the J1120+0641 binned spectrum, corrected with the 2σ clipping median flux of all pixels in the Lyα forest. Before calculating the covering fraction of dark pixels, we perform a visual inspection on every binned spectrum by comparing it with near-infrared sky OH emission lines (Rousselot et al. 2000). We manually mask any bright pixel plausibly caused by sky emission at $z > 6.3$ in the binned spectrum. These manually masked "sky" pixels are denoted by yellow hatched pixels in Figure 4.

We adopt a flux threshold method to identify "dark pixels" in the binned spectra, following McGreer et al. (2011). Pixels with flux density less than 2σ, where σ is the binned spectral uncertainty, are identified as "dark pixels." These dark pixels are denoted by black bars in Figure 4. McGreer et al. (2011, 2015) introduced an alternative definition of the "dark" pixel fraction as twice the fraction of pixels with negative flux. Since the "dark" pixels intrinsically have zero flux, there is a probability of 0.5 for them to scatter below 0 flux. We do not adopt this negative flux pixel definition because this method requires an extremely precise background subtraction, which is difficult to achieve for the highest redshift quasar spectra in this study due to the sky background (see Section 2). As dark pixel fractions are used as upper limits on $\bar{x}_{\mathrm{H\,I}}$, we then calculate the ratio of total number of dark pixels to the total number of pixels of all quasar lines of sight as the dark pixel fraction within a redshift bin of $\Delta z = 0.2$ for both the Lyα transition (from $z = 5.2$ to $z = 6.8$) and the Lyβ transition (from $z = 5.4$ to $z = 6.8$). In each redshift bin, we use jackknife statistics to derive the 1σ uncertainty in the dark pixel fraction.

Apart from the individual constraints from Lyα and Lyβ forests, we also derive a combined dark pixel fraction in Lyα and Lyβ forests from their redshift overlapping regions (McGreer et al. 2011). For this combined dark pixel fraction, we stack the spectral uncertainty in Lyα and Lyβ forests at the same redshift using the inverse variance weighting and utilize the stacked spectral uncertainty to put 3.3 cMpc pixels at local minima. The corresponding binned spectrum is shown in the lower middle panel in Figure 4. In this constraint, a pixel is

Table 1
Information of Quasar Optical Spectroscopy

ID (1)	Name (2)	z (3)	Telescope/Instrument (4)	Median $\tau^{\alpha}_{\mathrm{lim},2\sigma}$ (5)
1	J1120+0641	7.09	VLT/X-Shooter	5.23
2	J0252−0503	7.00	VLT/X-Shooter	4.76
3	J2211−6320	6.84	VLT/X-Shooter	3.73
4	J0020−3653	6.83	VLT/X-Shooter	3.77
5	J0319−1008	6.83	Gemini/GMOS	3.40
6	J0411−0907	6.81	LBT/MODS	2.78
7	J0109−3047	6.79	VLT/X-Shooter	3.05
8	J0218+0007	6.77	Keck/LRIS	2.95
9	J1104+2134	6.74	Keck/LRIS	4.33
10	J0910+1656	6.72	Keck/LRIS	3.34
11	J0837+4929	6.71	LBT/MODS	3.19
			MMT/BINOSPEC	
12	J1048−0109	6.68	VLT/X-Shooter	3.00
13	J2002−3013	6.67	Gemini/GMOS	3.98
14	J2232+2930	6.66	VLT/X-Shooter	4.04
15	J1216+4519	6.65	Gemini/GMOS	3.49
			Keck/LRIS	
			LBT/MODS	
16	J2102−1458	6.65	Keck/DEIMOS	3.36
17	J0024+3913	6.62	Keck/DEIMOS	4.08
18	J0305−3150	6.61	VLT/X-Shooter	3.48
19	J1526−2050	6.59	Keck/DEIMOS	4.56
20	J2132+1217	6.59	Keck/DEIMOS	4.71
21	J1135+5011	6.58	MMT/BINOSPEC	3.39
22	J0226+0302	6.54	Keck/DEIMOS	4.81
23	J0148−2826	6.54	Gemini/GMOS	2.73
24	J0224−4711	6.53	VLT/X-Shooter	3.98
25	J1629+2407	6.48	Keck/DEIMOS	4.20
26	J2318−3113	6.44	VLT/X-Shooter	3.93
27	J1148+5251	6.42	Keck/ESI	5.60
28	J0045+0901	6.42	Keck/DEIMOS	3.89
29	J1036−0232	6.38	Keck/DEIMOS	4.45
30	J1152+0055	6.36	VLT/X-Shooter	3.11
31	J1148+0702	6.34	VLT/X-Shooter	4.20
32	J0142−3327	6.34	VLT/X-Shooter	4.28
33	J0100+2802	6.33	VLT/X-Shooter	7.25
34	J1030+0524	6.31	Keck/ESI	5.64
			VLT/X-Shooter	
35	J1623+3112	6.25	Keck/ESI	3.95
36	J1319+0950	6.13	VLT/X-Shooter	5.27
37	J1509−1749	6.12	Magellan/MagE	4.92
			VLT/X-Shooter	
38	J0842+1218	6.08	Keck/ESI	3.75
39	J1630+4012	6.07	MMT/Red Channel Spectrograph	2.71
40	J0353+0104	6.05	Keck/ESI	3.15
41	J2054−0005	6.04	Magellan/MagE	4.29
42	J1137+3549	6.03	Keck/ESI	3.45
43	J0818+1722	6.02	MMT/Red Channel Spectrograph	5.42
			VLT/X-Shooter	
44	J1306+0356	6.02	Keck/ESI	5.04
			VLT/X-Shooter	
45	J0841+2905	5.98	Keck/ESI	3.13
46	J0148+0600	5.92	VLT/X-Shooter	5.80
47	J1411+1217	5.90	Keck/ESI	3.37
48	J1335+3533	5.90	Keck/ESI	3.22
49	J0840+5624	5.84	Keck/ESI	3.52
50	J0836+0054	5.81	Keck/ESI	5.56
			MMT/Red Channel Spectrograph	
			VLT/X-Shooter	

Table 1
(Continued)

ID (1)	Name (2)	z (3)	Telescope/Instrument (4)	Median $\tau^{\alpha}_{\mathrm{lim},2\sigma}$ (5)
51	J1044−0125	5.78	Magellan/MagE	4.74
52	J0927+2001	5.77	Keck/ESI	3.32
53	J1420−1602	5.73	Magellan/MagE	4.96

Note. (1) ID of quasar sight lines, in descending order of redshift. (2) Name of quasar. (3) Redshift. (4) Instrument used to obtain the spectrum. (5) The median of 2σ limiting optical depth in the Lyα forest, on a pixel scale of 3.3 cMpc. If there are multiple spectra of one object, the listed 2σ limiting optical depth is given for the stacked spectrum.
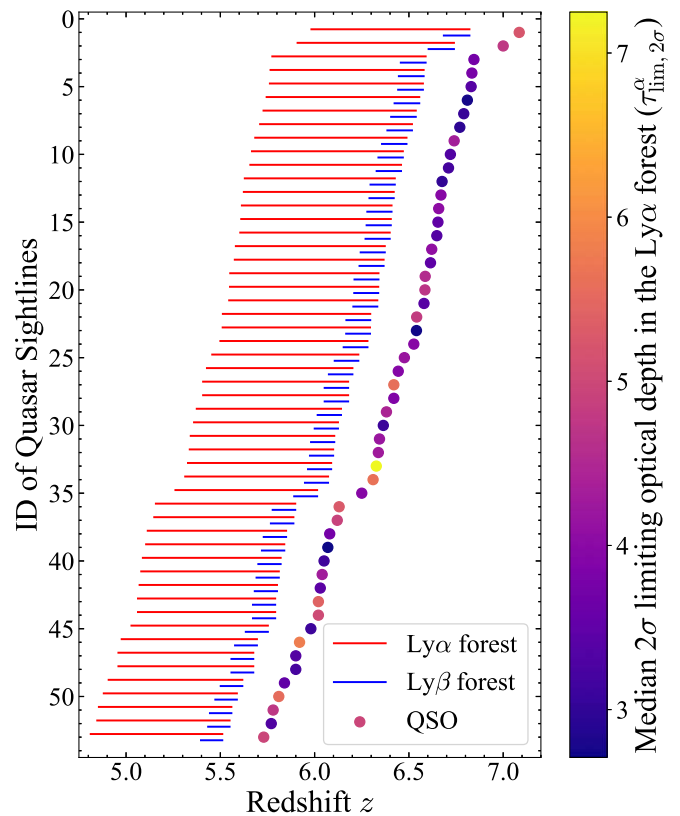

Figure 2. Redshift distribution of all quasars (circles) used in this study and the redshift ranges of their Lyα (red lines) and Lyβ forests (blue lines) used in our analysis. The corresponding optical spectroscopic information of a quasar sight line ID can be found in Table 1. The median 2σ limiting optical depth in the Lyα forest ($\tau^{\alpha}_{\mathrm{lim},2\sigma}$) of each quasar sight line is color coded and calculated in Section 3, showing the average depth in the Lyα forest. A higher median $\tau^{\alpha}_{\mathrm{lim},2\sigma}$ denotes that this quasar sight line is able to probe more opaque patches in the IGM.

"dark" only if its flux density is below 2σ binned spectral uncertainty in both the Lyα and Lyβ transitions. The redshift range used to calculate the dark pixel fraction for this combined constraint from Lyα and Lyβ forests is the same as the redshift range used to calculate the dark pixel fraction in Lyβ forests.

We perform a continuum fitting of the original spectrum by assuming a broken power law with a break at the rest frame 1000 Å (Shull et al. 2012). We use the least-squares method to
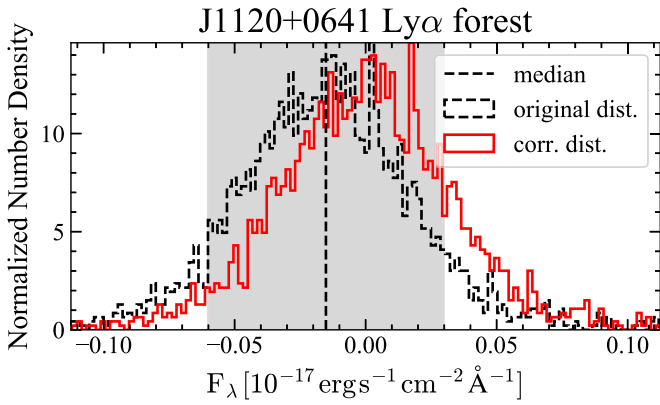
Figure 3. To correct "zero" flux level in VLT/X-Shooter spectra, we apply the median flux derived from sigma-clipped pixels to the VLT/X-Shooter spectra. The original flux distribution of pixels in the Lyα forest from the J1120+0641 VLT/X-Shooter spectrum is shown by the black histogram. The median derived from the sigma clipping is denoted by the vertical black dashed line, and the 2σ range from sigma clipping is in the gray shaded region. The flux distribution corrected by the sigma-clipped median is shown by the red histogram.

fit the spectrum within 1245–1285 and 1310–1380 Å[14] in the rest frame with a fixed spectral index (α_λ) of -1.5, following Yang et al. (2020a), and derive the normalization of the power-law continuum. We then calculate the continuum flux at rest frame $\lambda > 1000$ Å with the best-fit normalization and a spectral index of -1.5. At rest frame $\lambda < 1000$ Å, we switch the spectral index to $\alpha_\lambda = -0.59$ to calculate the continuum flux.

We calculate the 2σ limiting optical depth $\tau_{\rm lim,2\sigma} = -\ln(2\sigma/F_{\rm cont})$ for each 3.3 cMpc pixel where 2σ is the binned uncertainty on a pixel size of 3.3 cMpc and $F_{\rm cont}$ is the best-fit continuum flux. A higher limiting optical depth indicates that the pixel can place stronger constraints on the neutral hydrogen fraction in the IGM. We present the median limiting optical depth in the Lyα forest of the binned spectra (on a pixel scale of 3.3 cMpc) in Table 1. For pixels in Lyβ forests, we correct their limiting optical depth by subtracting the effective optical depth of foreground Lyα forests using the measured Lyα effective optical depth relations in Fan et al. (2006; for foreground Lyα forests at $z < 5.3$) and in Yang et al. (2020a; for foreground Lyα forests at $5.3 < z < 6.0$). When calculating the dark pixel fraction, we exclude $\tau_{\rm lim,2\sigma} < 2.5$ for Lyα pixels (i.e., $\tau^\alpha_{\rm lim,2\sigma} < 2.5$) as those pixels do not have enough sensitivity to probe the neutral hydrogen. Considering the Lyα and Lyβ transitions have different oscillator strengths, the corresponding cut in a limiting optical depth for Lyβ pixels will be $\tau^\beta_{\rm lim,2\sigma} < 2.50/2.19 \sim 1.14$, assuming a conversion factor of 2.19 between Lyα and Lyβ effective optical depth (Fan et al. 2006). Furthermore, we recalculate the dark pixel fraction only with $\tau^\alpha_{\rm lim,2\sigma} > 4.5$ pixels (corresponding to $\tau^\beta_{\rm lim,2\sigma} > 2.05$ for Lyβ pixels) to constrain the neutral hydrogen fraction with high-quality pixels.

4. Results and Discussion

We present the redshift evolution of upper limits on $\overline{x}_{\rm H\,I}$ from dark pixels in Figure 5. The number of $\tau^\alpha_{\rm lim,2\sigma} > 2.5$ pixels in each $\Delta z = 0.2$ bin in redshift, the number of lines of sight in each redshift bin, and the upper limits derived from

$\tau^\alpha_{\rm lim,2\sigma} > 2.5$ pixels are shown in the left panel, and the results of $\tau^\alpha_{\rm lim,2\sigma} > 4.5$ pixels are shown in the right panel. In both two panels, the combined dark pixel fractions from Lyα and Lyβ forests give the most stringent upper limits on $\overline{x}_{\rm H\,I}$. From the combined dark pixel fraction derived from $\tau^\alpha_{\rm lim,2\sigma} > 2.5$ pixels in Lyα and Lyβ forests, the upper limit on the neutral hydrogen is $18\% \pm 8\%$ at $z = 5.5$, and it increases to $69\% \pm 6\%$ at $z = 6.1$, $79\% \pm 4\%$ at $z = 6.3$, $87\% \pm 3\%$ at $z = 6.5$, and $94\%^{+6\%}_{-9\%}$ at $z = 6.7$. By adopting a higher limiting optical depth cut at 4.5 than at 2.5, the number of available pixels and the number of available quasar lines of sight drop significantly in each $\Delta z = 0.2$ redshift bin. Furthermore, the upper limit on $\overline{x}_{\rm H\,I}$ becomes tighter at $z < 6$. The upper limit on $\overline{x}_{\rm H\,I}$ is $9\% \pm 8\%$ at $z = 5.5$, $16\% \pm 14\%$ at $z = 5.7$, and $28\% \pm 8\%$ at $z = 5.9$. At $z > 6$, dark pixel fractions derived from $\tau^\alpha_{\rm lim,2\sigma} > 4.5$ pixels increase significantly, which can be caused by the rapid evolution in the IGM Lyα and Lyβ effective optical depth (e.g., Yang et al. 2020a). However, this rapid increase in the combined Lyα and Lyβ dark pixel fraction can also be associated with a small data sample, as only five quasar lines of sight are available with $\tau^\alpha_{\rm lim,2\sigma} > 4.5$ pixels at $z = 6.1$. Furthermore, at $z > 6$, dark pixel fractions derived from $\tau^\alpha_{\rm lim,2\sigma} > 4.5$ pixels do not necessarily provide more stringent upper limits on $\overline{x}_{\rm H\,I}$ than those derived from $\tau^\alpha_{\rm lim,2\sigma} > 2.5$ pixels. At $z > 6.3$, the number of available $\tau^\alpha_{\rm lim,2\sigma} > 4.5$ pixels is very limited. For example, at $z \sim 6.4$–6.6 (the central redshift of the bin is $z = 6.5$), there is no $\tau^\alpha_{\rm lim,2\sigma} > 4.5$ pixel in Lyβ forests due to the lack of high S/N quasar spectra and the narrow wavelength range of Lyβ forests used in our analysis. We tabulate the redshift distributions of the number of quasar lines of sight, the number dark pixels, the number of pixels, and the value of dark pixel fractions in Table 2.

We show our upper limits on the IGM neutral hydrogen fraction, along with other constraints on neutral hydrogen fractions from high-redshift quasars in Figure 6. Since the dark pixel fraction derived from $\tau^\alpha_{\rm lim,2\sigma} > 4.5$ pixels can provide tighter constraints on the neutral hydrogen fraction at $z < 6$, and at $z > 6$ the number of $\tau^\alpha_{\rm lim,2\sigma} > 2.5$ pixels is much higher than the number of $\tau^\alpha_{\rm lim,2\sigma} > 4.5$ pixels, we present the dark pixel fraction derived from $\tau^\alpha_{\rm lim,2\sigma} > 2.5$ pixels at $z > 6$, denoted by red upper limits. The dark pixel fraction calculated with $\tau^\alpha_{\rm lim,2\sigma} > 4.5$ pixels at $z < 6$ are denoted by magenta upper limits. The dark pixel fraction in McGreer et al. (2015) at $5.5 < z < 6.2$, derived from 22 quasars, are shown by blue upper limits. Our upper limits on the neutral fraction at $z < 6$ are slightly higher than the upper limits in McGreer et al. (2015). The possible reasons for this difference include (1) McGreer et al. (2015) double the covering fraction of negative pixels as the dark pixel fraction, while the dark pixel in this work is defined by 2σ flux threshold (McGreer et al. 2011), and (2) to avoid possible contamination from quasar proximity zones and intrinsic spectra, we adopt narrower wavelength ranges for both Lyα forests than the wavelength ranges used in McGreer et al. (2015). We repeat the results in McGreer et al. (2015) and test the above two factors in the resulted dark pixel fractions. We notice that the dark pixel definition (either dark pixels are defined by flux threshold or negative pixels) accounts for the major difference between our results and McGreer et al. (2015). Adopting a dark pixel definition of 2σ flux threshold, the combined Lyα and Lyβ dark pixel fractions in McGreer et al. (2015) will become 0.16 ± 0.08 at $z = 5.58$, 0.31 ± 0.10 at $z = 5.87$, and 0.63 ± 0.24 at $z = 6.07$, derived from $\tau^\alpha_{\rm lim,1\sigma} > 4.5$ (corresponding $\tau^\alpha_{\rm lim,2\sigma} > 3.8$) pixels. Although flux threshold

---

[14] For J0024+3913 and J2132+1217, only the wavelength range of 1245–1285 Å is used in the continuum fitting since the spectrum in 1310–1380 Å is noisy.
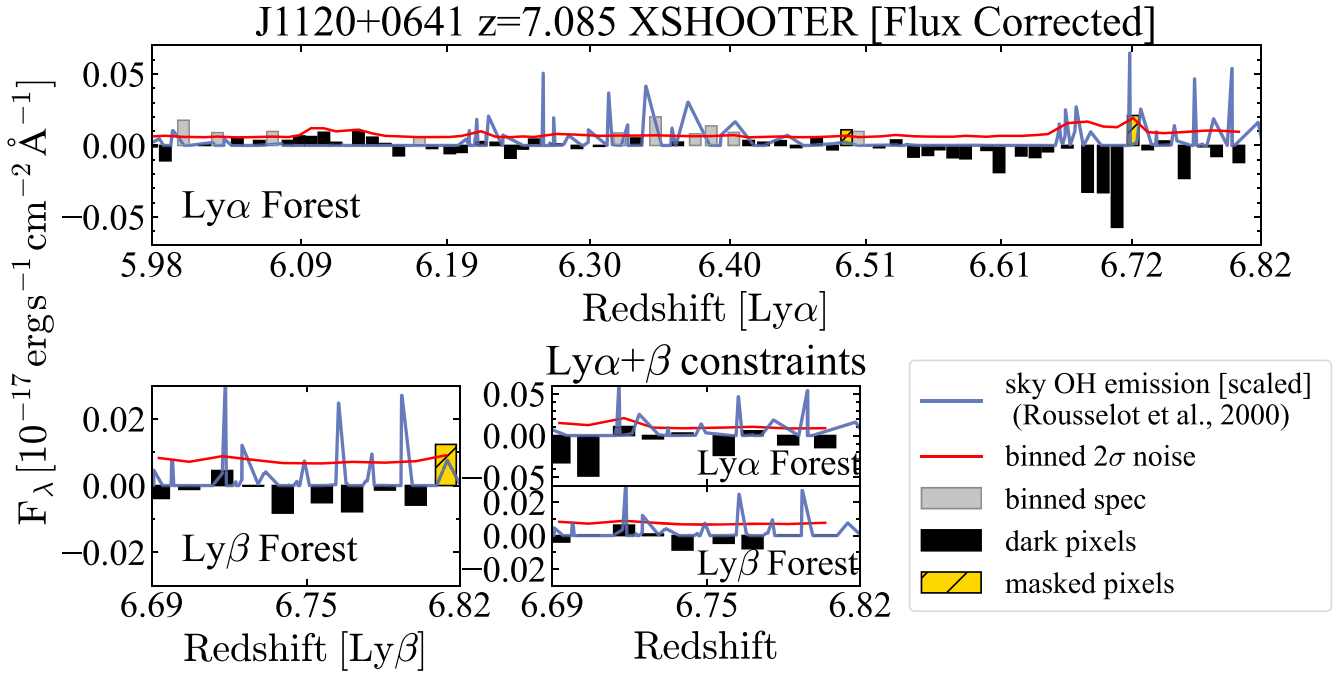
Figure 4. J1120+0641 binned spectrum in the Lyα forests (upper panel), Lyβ forests (lower left panel), and the redshift overlapping regions in Lyα and Lyβ forests (lower middle panel). The size of each binned pixel is 3.3 cMpc. The binned 2σ spectral uncertainty is shown as the red line. The binned flux density is presented in bars, and identified "dark" pixels are shown in black. The sky OH emission is shown by the blue line (Rousselot et al. 2000), and our spectral binning method effectively puts the majority of pixels between sky OH emission lines. Yellow hatched pixels are manually masked during our analysis as those fluxes are plausibly from residual sky OH emission. The zero flux level is corrected by the 2σ clipping median of all pixels in the Lyα forest (i.e., the vertical dashed line shown in Figure 3).
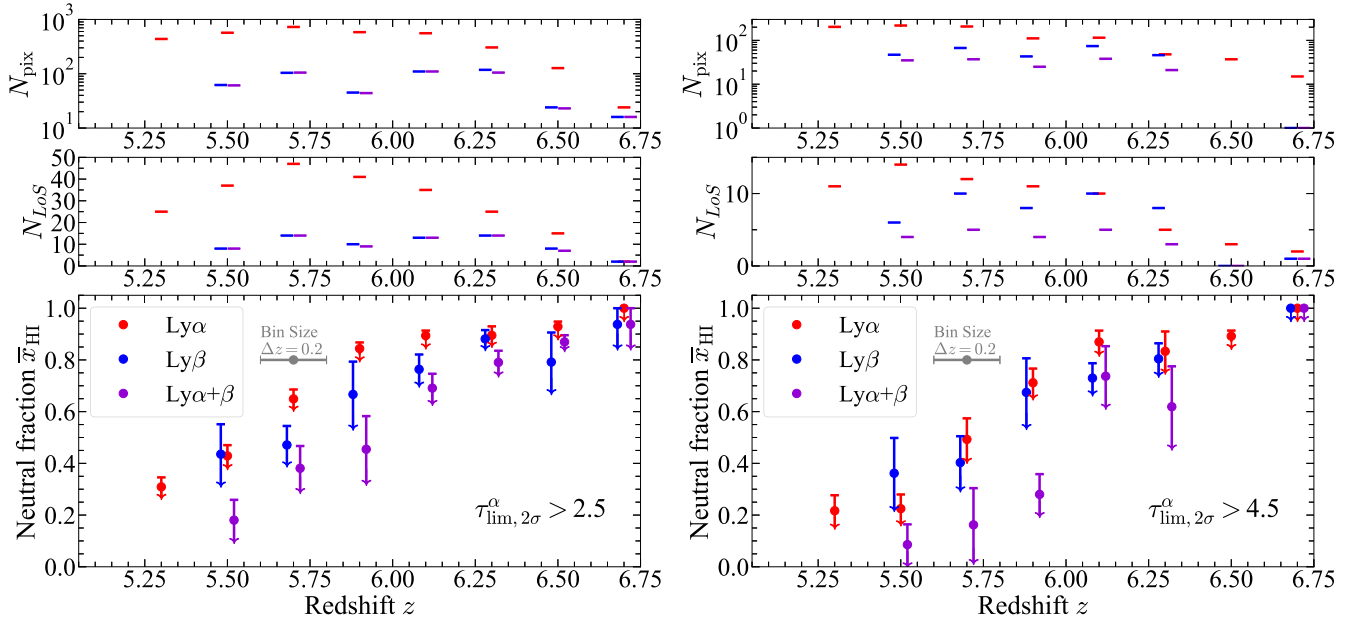
Figure 5. (Upper panels) Number of 3.3 cMpc pixels used to calculate the dark pixel fraction in the Lyα (red) and Lyβ (blue) forests, and the combined dark fraction in the Lyα and Lyβ forests (purple) in each bin of $\Delta z = 0.2$ in redshift. (Middle panels) Number of quasar lines of sight available in each bin of $\Delta z = 0.2$ in redshift. (Lower panels) Upper limits on the volume-averaged IGM neutral fraction $\bar{x}_{\rm H\,I}$ derived from the dark pixel fractions in the Lyα (red) and Lyβ (blue) forests as a function of redshift. The combined dark pixel fractions from the Lyα and Lyβ forests are denoted by purple markers. We adopt the same redshift bin ranges when calculating the dark pixel fractions derived from Lyα forests (red), Lyβ forests (blue), and combined Lyα and Lyβ forests (purple), but here we apply a small offset $\Delta z = 0.02$ in the figure for better visualization. The three panels on the left show the results with 3.3 cMpc pixels, of which the limiting optical depth is greater than 2.5; the three panels on the right are the results with 3.3 cMpc pixels, of which the limiting optical depth is greater than 4.5. Note there is no $\tau^{\alpha}_{\rm lim, 2\sigma} > 4.5$ pixel in the Lyβ forest in the $z = 6.5$ bin.

definition gives more conservative dark pixel fractions at $z < 6$, it is the only applicable method when deriving dark pixel fractions at the high-redshift end in this study, due to the strong sky emission.

In Figure 6, we show the upper limits on $\bar{x}_{\rm H\,I}$ from long dark gap size distributions in Lyα and Lyβ forests (Zhu et al. 2022), assuming a late reionization that ends at $z \lesssim 5.3$ (Nasir & D'Aloisio 2020). Our constraints at $z < 6$
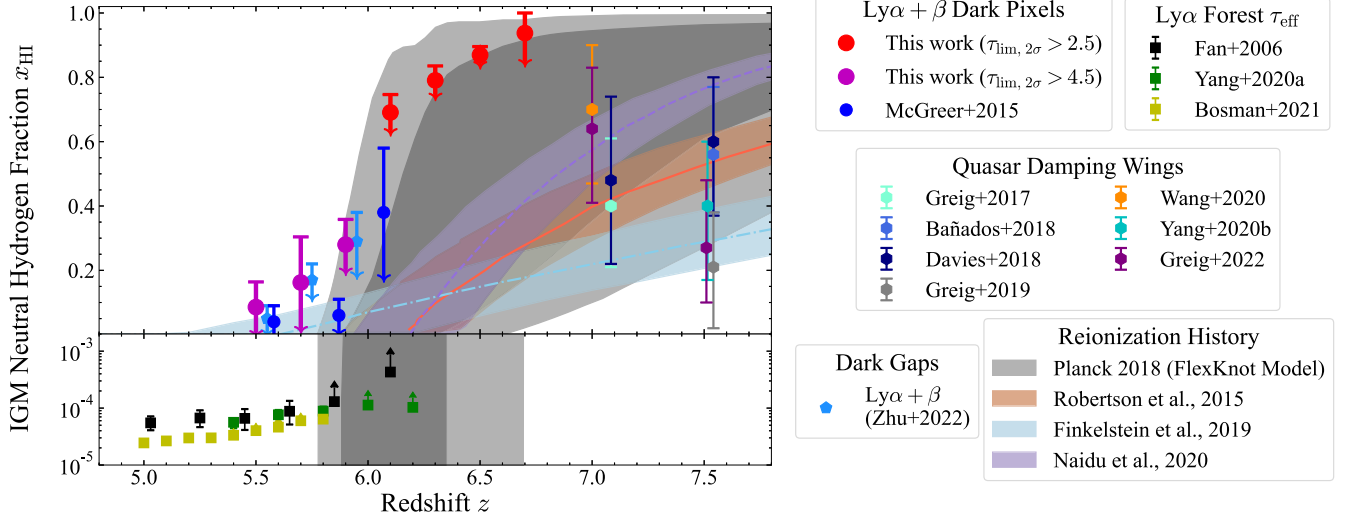
Figure 6. Constraints on the IGM neutral hydrogen fraction $\bar{x}_{\mathrm{H\,I}}$ from high-z quasar studies and Planck 2018 results. The upper limits on $\bar{x}_{\mathrm{H\,I}}$ from dark pixels are in red (this work, derived from flux-corrected $\tau^{\alpha}_{\mathrm{lim},2\sigma} > 2.5$ pixels at $z > 6$), magenta (this work, derived from flux-corrected $\tau^{\alpha}_{\mathrm{lim},2\sigma} > 4.5$ pixels at $z < 6$), and blue (McGreer et al. 2015). Constraints on $\bar{x}_{\mathrm{H\,I}}$ derived from Lyα effective optical depth are shown by black squares (Fan et al. 2006), green squares (Yang et al. 2020a), and yellow squares (Bosman et al. 2021). The upper limits on $\bar{x}_{\mathrm{H\,I}}$, inferred from long dark gap length distributions in Lyα and Lyβ forests, are shown in blue pentagons (Zhu et al. 2022). At $z > 7$, individual measurements on the neutral hydrogen fraction from quasar damping wings are denoted by hexagons (Greig et al. 2017, 2019; Bañados et al. 2018; Davies et al. 2018; Wang et al. 2020; Yang et al. 2020b). The 1σ and 2σ reionization history derived from the Planck 2018 results by assuming the FlexKnot model are denoted by the dark gray shaded region and the light gray shaded region (Planck Collaboration et al. 2020). The colored regions display 1σ reionization histories in Robertson et al. (2015; red), Finkelstein et al. (2019; blue), and Naidu et al. (2020; purple).

Table 2
Redshift Distribution of the Numbers of Quasar Lines of Sight, of Dark Pixels, of All Pixels, and Resulting Dark Pixel Fractions

Constraints	Redshift z	$\tau^{\alpha}_{\mathrm{lim},2\sigma} > 2.5$ pixels				$\tau^{\alpha}_{\mathrm{lim},2\sigma} > 4.5$ pixels			
		N_{LoS}	N_{dark}	N_{pix}	f_{dark}	N_{LoS}	N_{dark}	N_{pix}	f_{dark}
(1)	(2)	(3)	(4)	(5)	(6)	(7)	(8)	(9)	(10)
Lyα	5.3	25	135	437	0.31 ± 0.04	11	44	203	0.22 ± 0.06
	5.5	37	244	569	0.43 ± 0.04	14	49	218	0.22 ± 0.05
	5.7	47	472	727	0.65 ± 0.04	12	102	207	0.49 ± 0.08
	5.9	41	492	583	0.84 ± 0.02	11	79	111	0.71 ± 0.05
	6.1	35	498	557	0.89 ± 0.02	10	100	115	0.87 ± 0.04
	6.3	25	273	305	0.90 ± 0.03	5	40	48	0.83 ± 0.08
	6.5	15	118	127	0.93 ± 0.02	3	33	37	0.89 ± 0.02
	6.7	2	24	24	1.00	2	15	15	1.00
Lyβ	5.5	8	27	62	0.44 ± 0.12	6	17	47	0.36 ± 0.14
	5.7	14	49	104	0.47 ± 0.07	10	27	67	0.40 ± 0.10
	5.9	10	30	45	0.67 ± 0.13	8	29	43	0.67 ± 0.13
	6.1	13	84	110	0.76 ± 0.06	10	54	74	0.73 ± 0.06
	6.3	14	104	118	0.88 ± 0.03	8	37	46	0.80 ± 0.06
	6.5	8	19	24	0.79 ± 0.11	0	0	0	…
	6.7	2	15	16	$0.94^{+0.06}_{-0.09}$	1	1	1	1.00
Combined Lyα + Lyβ	5.5	8	11	61	0.18 ± 0.08	4	3	35	0.09 ± 0.08
	5.7	14	40	105	0.38 ± 0.09	5	6	37	0.16 ± 0.14
	5.9	9	20	44	0.45 ± 0.13	4	7	25	0.28 ± 0.08
	6.1	13	76	110	0.69 ± 0.06	5	28	38	0.74 ± 0.12
	6.3	14	83	105	0.79 ± 0.04	3	13	21	0.62 ± 0.16
	6.5	7	20	23	0.87 ± 0.03	0	0	0	…
	6.7	2	15	16	$0.94^{+0.06}_{-0.09}$	1	1	1	1.00

Note. (1) Type of dark pixel fractions. (2) Central redshift of each $\Delta z = 0.2$ bin. (3) The number of quasar lines of sight that have $\tau^{\alpha}_{\mathrm{lim},2\sigma} > 2.5$ pixels in this redshift bin. (4) The number of $\tau^{\alpha}_{\mathrm{lim},2\sigma} > 2.5$ dark pixels. (5) The total number of $\tau^{\alpha}_{\mathrm{lim},2\sigma} > 2.5$ pixels. (6) Dark pixel fraction derived from $\tau^{\alpha}_{\mathrm{lim},2\sigma} > 2.5$ pixels. (7) The number of quasar lines of sight that have $\tau^{\alpha}_{\mathrm{lim},2\sigma} > 4.5$ pixels in this redshift bin. (8) The number of $\tau^{\alpha}_{\mathrm{lim},2\sigma} > 4.5$ dark pixels. (9) The total number of $\tau^{\alpha}_{\mathrm{lim},2\sigma} > 4.5$ pixels. (10) Dark pixel fraction derived from $\tau^{\alpha}_{\mathrm{lim},2\sigma} > 4.5$ pixels. All the errors show 1σ confidence intervals.

are highly consistent with these upper limits derived from dark gap statistics. We also present constraints on $\bar{x}_{\mathrm{H\,I}}$ measured from the Lyα effective optical depth (Fan et al. 2006;

Yang et al. 2020a; Bosman et al. 2021). These $\bar{x}_{\mathrm{H\,I}}$ measurements from Lyα effective optical depth suggest the IGM is highly ionized and $\bar{x}_{\mathrm{H\,I}} \lesssim 10^{-4}$ at $z < 5.5$. At $z > 6$, the Lyα effective optical

depth measurements show that $\bar{x}_{\mathrm{H\,I}} \gtrsim 10^{-4}$ (Yang et al. 2020a). The IGM damping wing feature embedded in the $z > 7$ quasar spectra can be used to constrain the IGM neutral fraction, based on models of the IGM morphology and quasar intrinsic emission (e.g., Schroeder et al. 2013). In Figure 6, we show several recent measurements on neutral fraction at $z > 7$ from IGM damping wings in hexagons (Greig et al. 2017, 2019, 2022; Bañados et al. 2018; Davies et al. 2018; Wang et al. 2020; Yang et al. 2020b). Their medians show $\bar{x}_{\mathrm{H\,I}} \sim 0.2$–0.7, suggesting that the IGM is significantly neutral at $z \gtrsim 7$.

The reionization history, derived from the Planck 2018 results, assuming the FlexKnot model (Planck Collaboration et al. 2020), is shown by the dark gray shaded region (1σ confidence level) and the light gray shaded region (2σ confidence level). The FlexKnot model reconstructs the reionization history with an arbitrary number of knots, interpolates the reionization history between knots, and utilizes the Bayesian interference to marginalize the number of knots (Millea & Bouchet 2018). We also include 1σ reionization histories from Robertson et al. (2015; red region), Finkelstein et al. (2019; blue region), and Naidu et al. (2020; purple region). The ionizing budget during reionization is dominated by faint galaxies ($M_{\mathrm{UV}} > -15$) in Finkelstein et al. (2019), while the reionization photon budget in the models of Robertson et al. (2015) and Naidu et al. (2020) is dominated by bright galaxies. Our upper limits on neutral hydrogen fraction at $6.3 \lesssim z \lesssim 6.7$ are within the 1σ reionization history (assuming the FlexKnot model) from Planck 2018. However, the upper limits on $\bar{x}_{\mathrm{H\,I}}$ derived from dark pixels are not very efficient in distinguishing the other three reionization histories at $z > 6$ shown in Figure 6. This results from the limited number of quasar sight lines at $z > 6.8$ and the noisy sky background in the observed wavelength of interest, leading to a small number of pixels with high limiting optical depth at $z \gtrsim 6.5$. Deeper optical spectroscopy on existing $z > 6.8$ quasars and more quasar lines of sight at $z > 6.8$, as well as potential observations from space, are needed for future similar studies to generate more stringent constraints on $\bar{x}_{\mathrm{H\,I}}$ at $z > 6.5$.

5. Conclusion

In this paper, we present the dark pixel fractions in Lyα and Lyβ forests of 53 quasars at $5.73 < z < 7.09$. These dark pixel fractions provide the first model-independent upper limits on the volume-averaged IGM neutral fraction at $6.2 < z < 6.8$: $\bar{x}_{\mathrm{H\,I}}(z = 6.3) < 0.79 \pm 0.04$ (1σ), $\bar{x}_{\mathrm{H\,I}}(z = 6.5) < 0.87 \pm 0.03$ (1σ), and $\bar{x}_{\mathrm{H\,I}}(z = 6.7) < 0.94^{+0.06}_{-0.09}$ (1σ). The dark pixel fractions at $z < 6.1$ in this work are slightly higher than the dark pixel fractions presented in McGreer et al. (2015) due to a different definition of dark pixels used in this work and the selection of different wavelength ranges in Lyman series forests for dark pixel fraction calculation. We find that the dark pixel fractions at $z > 6.2$ are consistent with the 1σ IGM neutral fraction evolution derived from the Planck 2018 results when assuming the FlexKnot model (Planck Collaboration et al. 2020).

The current upper limits on $\bar{x}_{\mathrm{H\,I}}$, derived from dark pixels, are not stringent enough to distinguish various reionization histories (e.g., Robertson et al. 2015; Finkelstein et al. 2019; Naidu et al. 2020). The future improvement of similar dark pixel studies requires more quasar sight lines, deeper optical spectroscopy covering Lyman series forests, and observations

from space to exclude the potential contamination from sky OH emission lines.

ORCID iDs

Xiangyu Jin https://orcid.org/0000-0002-5768-738X
Jinyi Yang https://orcid.org/0000-0001-5287-4242
Xiaohui Fan https://orcid.org/0000-0003-3310-0131
Feige Wang https://orcid.org/0000-0002-7633-431X
Eduardo Bañados https://orcid.org/0000-0002-2931-7824
Fuyan Bian https://orcid.org/0000-0002-1620-0897
Frederick B. Davies https://orcid.org/0000-0003-0821-3644
Anna-Christina Eilers https://orcid.org/0000-0003-2895-6218
Emanuele Paolo Farina https://orcid.org/0000-0002-6822-2254
Joseph F. Hennawi https://orcid.org/0000-0002-7054-4332
Fabio Pacucci https://orcid.org/0000-0001-9879-7780
Bram Venemans https://orcid.org/0000-0001-9024-8322
Fabian Walter https://orcid.org/0000-0003-4793-7880

References

Astropy Collaboration, Price-Whelan, A. M., Lim, P. L., et al. 2022, ApJ, 935, 167
Astropy Collaboration, Price-Whelan, A. M., Sipőcz, B. M., et al. 2018, AJ, 156, 123
Astropy Collaboration, Robitaille, T. P., Tollerud, E. J., et al. 2013, A&A, 558, A33
Bañados, E., Venemans, B. P., Mazzucchelli, C., et al. 2018, Natur, 553, 473
Barnett, R., Warren, S. J., Becker, G. D., et al. 2017, A&A, 601, A16
Becker, G. D., Bolton, J. S., Madau, P., et al. 2015, MNRAS, 447, 3402
Becker, G. D., D'Aloisio, A., Christenson, H. M., et al. 2021, MNRAS, 508, 1853
Bosman, S. E. I., Ďurovčíková, D., Davies, F. B., & Eilers, A.-C. 2021, MNRAS, 503, 2077
Bosman, S. E. I., Fan, X., Jiang, L., et al. 2018, MNRAS, 479, 1055
Calverley, A. P., Becker, G. D., Haehnelt, M. G., & Bolton, J. S. 2011, MNRAS, 412, 2543
Carilli, C. L., Wang, R., Fan, X., et al. 2010, ApJ, 714, 834
Davies, F. B., Hennawi, J. F., Bañados, E., et al. 2018, ApJ, 864, 142
Eilers, A.-C., Davies, F. B., & Hennawi, J. F. 2018, ApJ, 864, 53
Eilers, A.-C., Davies, F. B., Hennawi, J. F., et al. 2017, ApJ, 840, 24
Eilers, A.-C., Hennawi, J. F., Davies, F. B., & Oñorbe, J. 2019, ApJ, 881, 23
Fan, X., Strauss, M. A., Becker, R. H., et al. 2006, AJ, 132, 117
Finkelstein, S. L., D'Aloisio, A., Paardekooper, J.-P., et al. 2019, ApJ, 879, 36
Greig, B., Mesinger, A., & Bañados, E. 2019, MNRAS, 484, 5094
Greig, B., Mesinger, A., Davies, F. B., et al. 2022, MNRAS, 512, 5390
Greig, B., Mesinger, A., Haiman, Z., & Simcoe, R. A. 2017, MNRAS, 466, 4239
Harris, C. R., Millman, K. J., van der Walt, S. J., et al. 2020, Natur, 585, 357
Hoag, A., Bradač, M., Huang, K., et al. 2019, ApJ, 878, 12
Hunter, J. D. 2007, CSE, 9, 90
Itoh, R., Ouchi, M., Zhang, H., et al. 2018, ApJ, 867, 46
Jung, I., Finkelstein, S. L., Dickinson, M., et al. 2020, ApJ, 904, 144
Konno, A., Ouchi, M., Ono, Y., et al. 2014, ApJ, 797, 16
Konno, A., Ouchi, M., Shibuya, T., et al. 2018, PASJ, 70, S16
Mason, C. A., Fontana, A., Treu, T., et al. 2019, MNRAS, 485, 3947
Mason, C. A., Treu, T., Dijkstra, M., et al. 2018, ApJ, 856, 2
McGreer, I. D., Mesinger, A., & D'Odorico, V. 2015, MNRAS, 447, 499
McGreer, I. D., Mesinger, A., & Fan, X. 2011, MNRAS, 415, 3237
Mesinger, A. 2010, MNRAS, 407, 1328
Millea, M., & Bouchet, F. 2018, A&A, 617, A96
Miralda-Escudé, J. 1998, ApJ, 501, 15
Morales, A. M., Mason, C. A., Bruton, S., et al. 2021, ApJ, 919, 120
Mortlock, D. J., Warren, S. J., Venemans, B. P., et al. 2011, Natur, 474, 616
Naidu, R. P., Tacchella, S., Mason, C. A., et al. 2020, ApJ, 892, 109
Nasir, F., & D'Aloisio, A. 2020, MNRAS, 494, 3080
Osterbrock, D. E., Fulbright, J. P., Martel, A. R., et al. 1996, PASP, 108, 277
Ouchi, M., Harikane, Y., Shibuya, T., et al. 2018, PASJ, 70, S13
Pentericci, L., Fontana, A., Vanzella, E., et al. 2011, ApJ, 743, 132
Planck Collaboration, Aghanim, N., Akrami, Y., et al. 2020, A&A, 641, A6
Prochaska, J., Hennawi, J., Westfall, K., et al. 2020a, JOSS, 5, 2308
Prochaska, J. X., Hennawi, J., Cooke, R., et al. 2020b, pypeit/PypeIt: Release 1.0.0, v1.0.0, Zenodo, doi:10.5281/zenodo.3743493
Robertson, B. E., Ellis, R. S., Furlanetto, S. R., & Dunlop, J. S. 2015, ApJL, 802, L19
Rousselot, P., Lidman, C., Cuby, J. G., Moreels, G., & Monnet, G. 2000, A&A, 354, 1134
Schenker, M. A., Ellis, R. S., Konidaris, N. P., & Stark, D. P. 2014, ApJ, 795, 20
Schroeder, J., Mesinger, A., & Haiman, Z. 2013, MNRAS, 428, 3058
Shull, J. M., Stevens, M., & Danforth, C. W. 2012, ApJ, 752, 162
Sobacchi, E., & Mesinger, A. 2015, MNRAS, 453, 1843
Stark, D. P., Ellis, R. S., Chiu, K., Ouchi, M., & Bunker, A. 2010, MNRAS, 408, 1628
Venemans, B. P., Bañados, E., Decarli, R., et al. 2015, ApJL, 801, L11
Virtanen, P., Gommers, R., Oliphant, T. E., et al. 2020, NatMe, 17, 261
Wang, F., Davies, F. B., Yang, J., et al. 2020, ApJ, 896, 23
Worseck, G., Prochaska, J. X., O'Meara, J. M., et al. 2014, MNRAS, 445, 1745
Yang, J., Wang, F., Fan, X., et al. 2020a, ApJ, 904, 26
Yang, J., Wang, F., Fan, X., et al. 2020b, ApJL, 897, L14
Zhu, Y., Becker, G. D., Bosman, S. E. I., et al. 2021, ApJ, 923, 223
Zhu, Y., Becker, G. D., Bosman, S. E. I., et al. 2022, ApJ, 932, 76